Investigation of cavitation and vapor shedding mechanisms in a Venturi nozzle

Maxwell Brunhart[1,a], Celia Soteriou[1], Manolis Gavaises[2],
Ioannis Karathanassis[2], Phoevos Koukouvinis[2], Saad Jahangir[3] and Christian Poelma[3]

[1]*Delphi Technologies, Gillingham ME8 0RU, UK*
[2]*City, University of London, London EC1V 0HB, UK*
[3]*Delft University of Technology, 2600 AA Delft, Netherlands*

[a]Author to whom correspondence should be addressed: maxwell.brunhart@city.ac.uk

Abstract

Cavitating flow dynamics are investigated in an axisymmetric converging-diverging Venturi nozzle. Computational Fluid Dynamics (CFD) results are compared with those from previous experiments. New analysis performed on the quantitative results from both data sets reveals a coherent trend and show that the simulations and experiments agree well. The CFD results have confirmed the interpretation of the high-speed images of the Venturi flow, which indicated there are two vapor shedding mechanisms that exist under different running conditions: re-entrant jet and condensation shock. Moreover, they provide further detail of the flow mechanisms that cannot be extracted from the experiments. For the first time with this cavitating Venturi nozzle, the re-entrant jet shedding mechanism is reliably achieved in CFD simulations. The condensation shock shedding mechanism is also confirmed, and details of the process are presented. These CFD results compare well with the experimental shadowgraphs, space-time plots and time-averaged reconstructed computed tomography (CT) slices of vapor fraction.

Keywords: cavitation, partial cavitation, CFD, Venturi, re-entrant jet, condensation shock

Nomenclature			
B	Bulk modulus factor (Pa)	$CN = \Delta p/(p_d - p_v)$	(Bergwerk) Cavitation number
C	Isentropic constant	$K = 2\Delta p/\rho\bar{u}^2$	Loss factor
c	Speed of sound (m/s)	$Re = \bar{u}D/\upsilon$	Reynolds Number
D	Characteristic length (m)	$St_d = fD/\bar{u}$	Strouhal number
f	Frequency (Hz)	$\Delta p = p_u - p_d$	Pressure drop (Pa)
p	Pressure (Pa)	$\lambda = \sqrt{10}Re^{-1/2}D$	Taylor length scale (m)
s	Wave speed (m/s)	$\sigma = 2(p_d - p_v)/\rho\bar{u}^2$	(Thoma) Cavitation number
t	Time (s)	$\tau = \sqrt{\upsilon/\varepsilon}$	Kolmogorov time scale (s)
u	Axial velocity component (m/s)	Subscripts	
$\bar{u}$	Average velocity (m/s)	d	Downstream
$\boldsymbol{U}$	Velocity vector field (m/s)	l	Liquid
γ	Heat capacity ratio	$post$	Post-shock
$\varepsilon \sim U^3/D$	Turbulent dissipation (m^2/s^3)	pre	Pre-shock
μ	Dynamic viscosity (Pa·s)	ref	reference
ρ	Density (kg/m^3)	sat	saturated
$\bar{\bar{\boldsymbol{\tau}}}$	Stress tensor (Pa)	u	Upstream
υ	Kinematic viscosity (m^2/s)	v	vapor

1 - Introduction

Hydrodynamic cavitation develops in regions of flow fields subjected to pressures lower than the working fluid vapor pressure. It can occur in a wide range of systems, such as those involving hydrofoils, in turbo machinery, as well as in orifices present in rocket and automotive fuel injectors [1]. The cavities may exist as large voids

or as clouds of bubbles and can be attached to a wall or travel in the mainstream flow [2]. Attached cavities can exhibit an unsteady trailing edge that oscillates or sheds vapor, which is carried downstream in the flow. These vapor formations and oscillations can result in negative effects on the system, like vibration, noise, loss of lift and power, and erosion [3]. When designing new systems, potential cavitation shedding must be understood so the system can be designed to cope with or avoid instabilities, and so function as needed. This is especially true for systems where cavitation is unavoidable, such as in high pressure fuel injectors [4] or ships propellers [5]. Having reliable CFD simulations would enable a fast turnaround for design optimization and would provide further details over the experimental results of the transient processes.

Experiments have generally shown that there are two mechanisms that lead to bulk vapor shedding and occur under different flow conditions. One is termed re-entrant jet and typically occurs when the attached or partial cavity is relatively short: a re-entrant flow from the cavity closure region extends back to the cavity start and causes the vapor to be pinched off and shed. This has been well documented by Knapp [6] and Furness & Hutton [7] in earlier years, and more recently by Foeth et al [8]. Further experimental studies have been conducted on the re-entrant jet velocity by Pham et al [9] and Stanley et al [10] and on the effects of obstructing the jet by Kawanami et al [11].

The other shedding mechanism is termed condensation or bubbly shock and typically occurs when the running conditions have enabled the attached vapor region to extend further downstream. The phenomenon was first suggested by Jakobsen [12], and can be triggered when a pressure wave, produced downstream from the collapse of previously shed vapor, propagates back upstream. When this wave arrives back at the trailing edge of the attached vapor, it triggers a condensation shock front. This front travels back up the attached vapor region, causing the vapor progressively to detach and partially collapse as it transitions to a shed vapor cloud. This mechanism has been well studied on wedges and other pseudo two-dimensional geometries by Campbell & Pitcher [13], Riesman et al [14], Laberteaux & Ceccio [15] and more recently by Wang et al [16] and numerically by Budich et al [17].

The two shedding mechanisms are well documented on hydrofoils. Arabnejad et al [18] investigated the re-entrant jet shedding mechanism on a NACA 0009 hydrofoil, both by experimental means and by simulations. They were able to demonstrate good agreement between the CFD and the experimental data in terms of shedding frequency, cavity length and overall vapor structure. The transition between the different shedding mechanisms was shown well by Arndt et al [19] who studied a NACA 0015 hydrofoil, also by experimental and numerical means. The researchers were able to demonstrate a sharp change in the shedding mechanism by changing either the cavitation number or angle of attack, which altered the amount of vapor produced.

Both shedding mechanisms have also been documented on a wedge, for example by Ganesh et al [20]. These researchers used time-averaged X-ray densitometry to illustrate both the re-entrant jet and condensation shock shedding mechanism. For the condensation shock mechanism, they showed the shock front moving back through the attached vapor region. Once the wave reached the wedge apex, the remaining vapor was shed downstream, and the process repeated.

The wedge used by Ganesh et al [20] was investigated with CFD by Budich et al [17]. Their investigation focused on the condensation shock regime, and they achieved good correlation in terms of shedding frequency and cavitation distribution with the experimental data. However, their results showed a significantly higher pressure drop than in the experiments. They attributed this in part to the two-phase model chosen which inhibited pressure recovery.

Trummler et al [21], following work by Sou et al [22], and Bicer and Sou [23], studied the two shedding mechanisms in an asymmetric, rectangular cross-section orifice. While not investigating the shedding frequencies, the authors were able to model the two shedding mechanisms using Large-Eddy Simulations (LES).

The shedding mechanisms were also investigated in an axisymmetric converging-diverging Venturi nozzle. Hogendoorn [24] and Jahangir et al [25] used high-speed imaging at different flow conditions and characterized a re-entrant jet shedding regime, a condensation shock shedding regime and a transition zone between them. When there was a small amount of vapor present near the orifice throat, they identified the shedding mechanism as re-entrant jet. As the running conditions were changed to produce more vapor, they reported that the shedding mechanism transitioned to condensation shock. They found that the re-entrant jet shedding mechanism had a much higher shedding frequency than the condensation shock mechanism. Jahangir et al [26] went on to collect time-averaged X-ray computed tomography (CT) data of the Venturi at two running conditions which were expected to produce the two shedding mechanisms. With this, the authors explored the averaged internal cavitation structures and the vapor distribution.

The Venturi nozzle used by Jahangir et al [25] was investigated with CFD in a Master Thesis by Cointe [27]. This work showed some vapor contours that appeared to distinguish the different shedding mechanisms but did not demonstrate the relatively high shedding frequencies for the re-entrant jet mechanism. Moreover, as in the work of Budich et al [17], they were also unable to produce the pressure drops that were seen in experiments.

The novelty in the work presented here exists firstly in the new, in-depth analysis revealing a more coherent trend in the quantitative results for the experiments over a wide range of running conditions. The quantitative CFD results match this trend. Facilitated by the in-depth analysis of the quantitative results, the CFD simulations achieve both the re-entrant jet and the condensation shock vapor shedding mechanisms, as seen in the experiments. Previous CFD investigations have had difficulty realizing the re-entrant jet case on this geometry [27] [28]. In addition, the current work clarifies the shedding mechanisms for internal three-dimensional geometries of circular cross-section, instead of simplified, often two-dimensional geometries, such as the frequently used wedge [17] [20] [29] [30] [31]. Further to that and for the first time on this geometry, average vapor fraction slices of the CFD are compared with those from the experimental computed tomography (CT) and show good agreement overall. Finally, details have been exposed which cannot be extracted from the experiments and provide additional insight into the shedding mechanisms.

For the current work, results are presented of the CFD investigation that was carried out on a Venturi nozzle, which has been studied experimentally. The simulation methodology is presented in section 2, while section 3 analyzes the CFD results and discusses how they compared to the experimental data. Finally, the summary and conclusion are given in section 4.

2 - Simulation methodology

The CFD simulations were run in ANSYS Fluent and solved the standard equations for mass (Eq. 1) and momentum (Eq. 2) conservation:

$$\frac{\partial \rho}{\partial t} + \boldsymbol{\nabla} \cdot (\rho\, \boldsymbol{U}) = 0 \qquad \text{Eq. 1}$$

$$\frac{\partial (\rho \boldsymbol{U})}{\partial t} + \boldsymbol{\nabla} \cdot (\rho \boldsymbol{U}\boldsymbol{U}) = -\boldsymbol{\nabla} p + \boldsymbol{\nabla} \cdot (\bar{\bar{\boldsymbol{\tau}}}) \qquad \text{Eq. 2}$$

where $\boldsymbol{U}$ is the velocity vector field, t is time, p is pressure, ρ is the density and $\bar{\bar{\boldsymbol{\tau}}}$ is the stress tensor.

The working fluid was modeled as water, water vapor and the mixture of the two. The equations of state (EoS) for each phase were implemented together as a barotropic single-fluid model, run with a user defined function (UDF). The three phases are compressible, which enables pressure wave propagation. These EoS have been

used by a number of authors [32] [33] and shown to be robust. A Tait EoS was used in the liquid phase (Eq. 3), an isentropic EoS for the vapor phase (Eq. 5), and an EoS based on Wallis speed of sound [34] when both the liquid and vapor were present (Eq. 4). The complete set of equations is given as:

$$p(\rho) = B\left[\left(\frac{\rho}{\rho_l}\right)^{7.15} - 1\right] + p_{sat,l} \qquad if \quad \rho \geq \rho_l \qquad \text{Eq. 3}$$

$$p(\rho) = \frac{c_v^2 c_l^2 \rho_l \rho_v (\rho_v - \rho_l)}{c_v^2 \rho_v^2 - c_l^2 \rho_l^2} \ln\left(\frac{\rho}{c_l^2 \rho_l (\rho_l - \rho) + c_v^2 \rho_v (\rho - \rho_v)}\right) + p_{ref} \quad if \quad \rho_l > \rho \geq \rho_v \qquad \text{Eq. 4}$$

$$p(\rho) = C\rho^{\gamma} \qquad if \quad \rho_v > \rho \qquad \text{Eq. 5}$$

where B is a factor that relates to the bulk modulus (actual bulk modulus is $7.15B$), C is a constant, γ is the heat capacity ratio, and v and l indicate vapor and liquid, respectively. Reference values p_{sat} and p_{ref} are used to ensure the equations are continuous. In Table 1, values of the EoS variables are provided for 16.5°C, the average running temperature of the experiments. As a reference, the density and speed of sound are plotted against pressure (Fig. 1).

Table 1 – Reference properties used for the EoS

Liquid properties	Values	Units	Vapor properties	Values	Units
B	307.3×10^{6}	Pa	γ	1.33	-
ρ_l	998.8	kg/m^3	C	27715	N/A
c_l	1472	m/s	ρ_v	1.41×10^{-2}	kg/m^3
μ_l	1.1×10^{-3}	Pa·s	c_v	95.4	m/s
$p_{sat,l}$	3659	Pa	μ_v	9.94×10^{-6}	Pa·s
p_{ref}	4280	Pa	$p_{sat,v}$	96.5	Pa

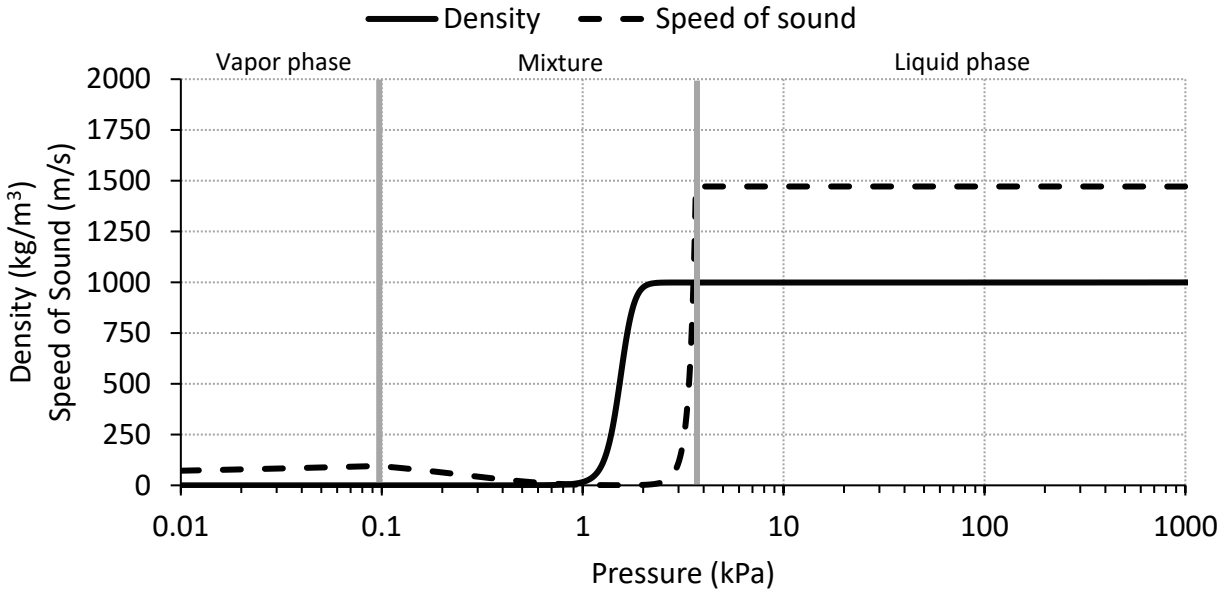

Fig. 1 – The density and speed of sound characteristics of the EoS plotted against pressure.

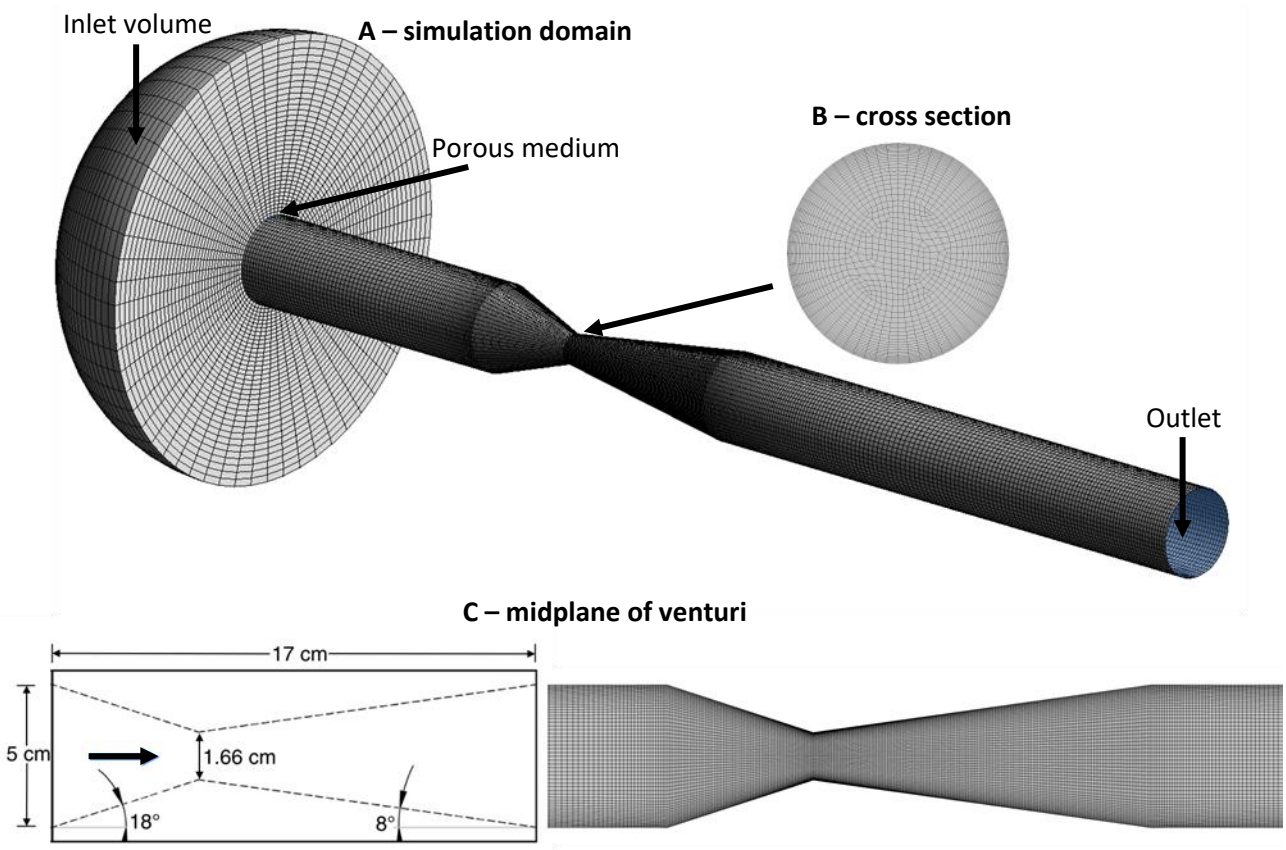

Fig. 2 – A: Mesh used for the simulations. B: cross-section of the mesh at the throat. C: Schematic of the Venturi nozzle geometry along with a mid-plane view of the mesh.

Throughout the different flow conditions and across the different diameters, the Reynolds number ranged from 7×10^4 to 2.5×10^5, which indicates that the flow is inertia dominated overall, rather than viscous dominated. As such, Cointe [27] used an inviscid model to simulate the Venturi nozzle flow, as did Budich et al [17] for simulations of flow over a wedge. Nevertheless, flow separation and low velocities are present in the diverging section of the nozzle. So as the viscosity could affect the shedding behavior, the Scale-Adaptive Simulation (SAS) turbulence model was selected for the current work, as described in [35] and [36]. This model is based on Unsteady Reynolds Averaged Navier-Stokes (URANS) but employs the von Karman length-scale and resolves smaller scale eddies than traditional URANS. The SAS turbulence model is classified as a scale resolving simulation (SRS) and so does not average the variables, but instead filters them. However, the filtering is not wholly based on the computational grid. In resolving more turbulent eddies, SAS provides a more detailed flow structure without necessarily requiring a greatly refined mesh and the large computational cost of LES.

The Venturi (Fig. 2) is 17cm in length with a throat diameter of 1.66cm. The upstream and downstream pipes have a diameter of 50mm. The mesh (Fig. 2) consisted of 8.2×10^5 cells with a cell axial length of 0.8mm near the Venturi throat. Coupled with a timestep of 1µs, the Courant–Friedrichs–Lewy condition (CFL) is less than 0.02 when considering the flow velocity at the throat. As pressure waves are a central feature of shedding, the acoustic CFL was also considered and equates to 1.75 in pure water. However, in mixture regions the speed of sound drops greatly [3] [34] and so the acoustic CFL in these regions is well below unity, in which case any pressure waves would be captured.

As a reference, the Taylor length scale is estimated to be 100µm and the Kolmogorov time scale is about 2µs. Hence the mesh could be further refined, but a well-structured tetrahedral mesh would need almost 20 million cells to achieve that level of refinement. In order to avoid the heavy computational cost associated with this,

the SAS model was allowed to revert back to URANS in the boundary layer. As such, the Y+ in the Venturi nozzle was usually below 30. However, the mesh is considerably finer than that implemented in other studies of this geometry [27] [28]. Coarser meshes were tested and resulted in similar flow characteristics and shedding, but worse Y+, so the finest mesh was used. Mesh suitability was confirmed when checks showed the simulated pressure drop vs flow rate matched the experiments (section 3.1).

Fig. 2 shows that the domain included an inlet volume followed by a porous medium boundary at the start of the inlet pipe (as suggested in [37] [38]). The values used for the porous medium boundary were 10^{10}m^2 for the permeability, 23m^{-1} for the pressure-lump coefficient and 1m for the thickness. The porous medium boundary works in a similar way to a snubber valve, used in high pressure fuel lines to reduce the effects of pressure reflections. The dimensions for the porous medium were selected from experience with snubber valves [39]. The upstream pressure was recorded downstream of the inlet volume, so that any pressure drop created by the porous medium did not impact the pressure readings used for the calculations. The simulations used a velocity boundary condition at the inlet and a fixed pressure at the outlet.

2.1 - Analysis of data

To understand any trends and to compare the experimental and CFD results, the following nondimensional numbers were used. Relating to the shedding frequency, the Strouhal number (St_d) is defined as:

$$St_d = \frac{fD}{\bar{u}} \qquad \text{Eq. 6}$$

where f is the shedding frequency, D is the characteristic length taken as the throat diameter and $\bar{u}$ is the average velocity at the throat.

Cavitation numbers of different definitions have long been used to indicate the level of vapor present in the flow. Jahangir et al [25] considered St_d with respect to a cavitation number (σ), given as:

$$\sigma = \frac{p_d - p_v}{\frac{1}{2}\rho\bar{u}^2} \qquad \text{Eq. 7}$$

where p_d is the downstream pressure, p_v is the vapor pressure and ρ is the reference liquid density. The downstream pressure was measured at 400mm from the throat in the CFD and 730mm in the experiments, a difference not considered significant as both locations are sufficiently far downstream and viscous losses were low, in the region of 0.2% of the overall pressure drop.

An alternative cavitation number, from the work of Bergwerk [40], was introduced to the analysis for the current work:

$$CN = \frac{\Delta p}{p_d - p_v} \qquad \text{Eq. 8}$$

where Δp is the difference between the upstream and downstream pressures. The upstream pressure was measured at 200mm from the throat in the CFD and 310mm in the experiments. Again, a difference not considered significant. This cavitation number is more consistently used for internal flows within industry (see for example [41] [42] [43] [44]) and takes into account the pressure drop caused by the feature of interest, which is not considered in σ. Moreover, the usual definition of σ [1] states that the velocity and pressure are taken at $\boldsymbol{U}_\infty$ and p_∞, respectively, which correspond to locations unaffected by the feature of interest, which is only reasonable when the flow is external.

The loss factor (K) was also considered:

$$K = \frac{\Delta p}{\frac{1}{2}\rho \bar{u}^2} \qquad \text{Eq. 9}$$

Normally K is considered for minor losses and is calculated with the average downstream velocity [41] [45], but here the average throat velocity was used to maintain consistency with relevant previous papers [25] [26].

3 - Results and discussion

3.1 - Quantitative results

The base experimental information comes from Hogendoorn [24] and Jahangir et al [25], who collected data for many running conditions for this Venturi nozzle. The quantitative experimental results were originally examined with respect to the cavitation number σ [25]. For the current work those results, along with the new CFD results, were also considered with respect to the cavitation number *CN*.

Fig. 3 shows the distribution of St_d with respect to both cavitation numbers. The regions of the two different shedding regimes, as determined by the experimental and CFD images (see sections 3.2 and 3.3), are indicated. As previously mentioned, cavitation numbers are used to indicate the level of vapor present in the flow: vapor levels increase as σ decreases or as *CN* increases. Hence when there is less vapor, as indicated in Fig. 3 by higher values of σ or lower values of *CN*, the shedding mechanism is predominantly re-entrant jet and sheds at a higher frequency. When there is more vapor (indicated by lower σ values or higher *CN* values), the dominant shedding mechanism is condensation shock and is characterized by a lower shedding frequency.

When St_d is plotted against *CN* (right plot in Fig. 3) the experimental results are much more cohesive and the same is true for the CFD results. Moreover, the two sets of results show good agreement with each other. This clearer result is consistent with *CN* being the cavitation number more appropriate for the internal, three-dimensional geometry tested in this work as it accounts for the pressure drop across the region of interest. It is also apparent from Fig. 3 that the re-entrant jet shedding mechanism is only possible over a very narrow range of running conditions. This feature, clearly shown in this in-depth analysis of the experimental and CFD results, has not been mentioned in past publications. This indicates why it has been difficult for past studies [27] [28] to simulate the re-entrant jet shedding mechanism.

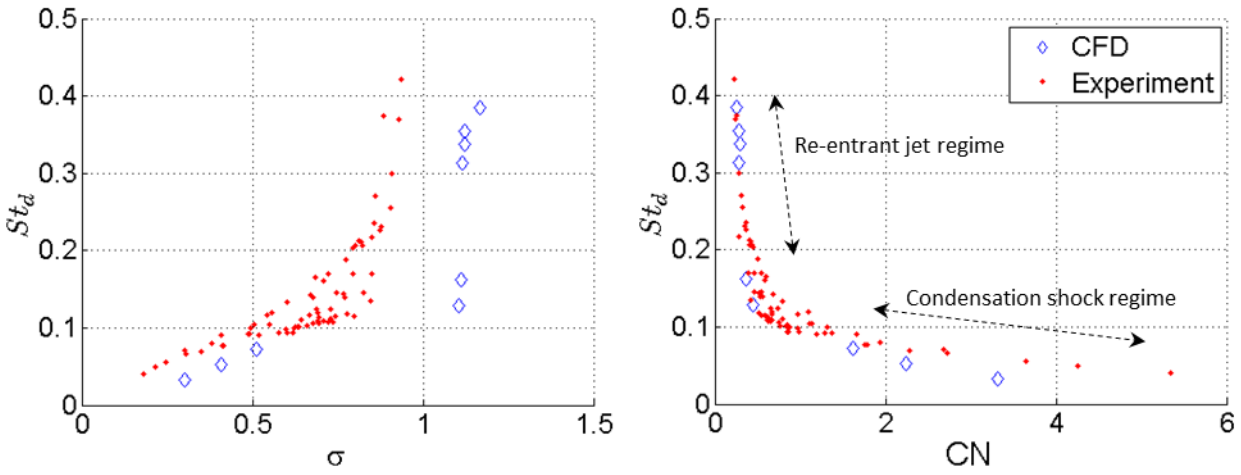

Fig. 3 – Strouhal number (St_d) versus different cavitation numbers. Left: σ. Right: *CN*.

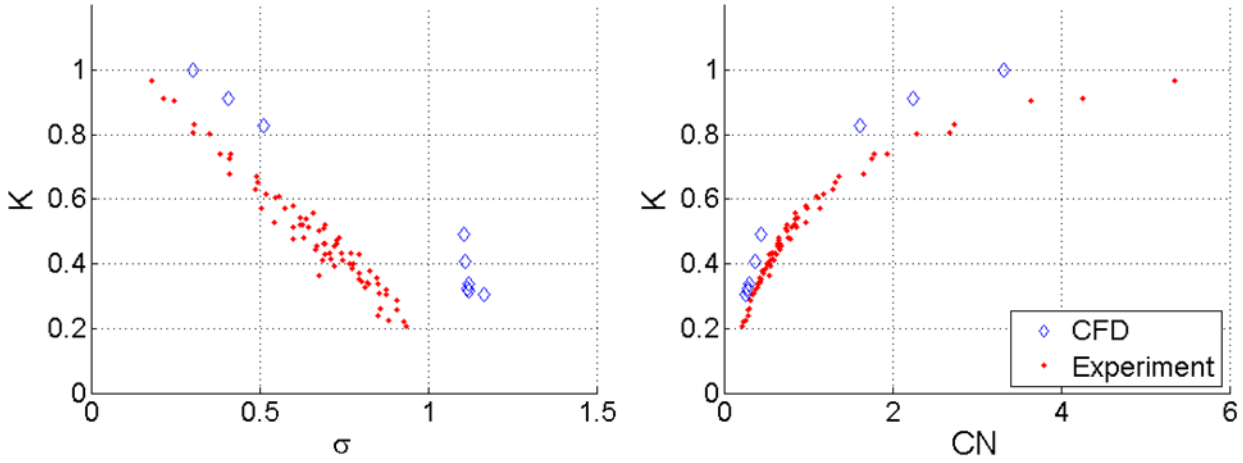

Fig. 4 – Loss factor (*K*) versus different cavitation numbers. Left: *σ*, Right: *CN*.

In Fig. 4, the loss factor (*K*) is plotted against σ and *CN*. Again, both the experimental and the CFD results are more cohesive when analyzed with respect to CN. It also shows that there is slightly more pressure loss in the CFD simulations. This is in line with other studies (see [17] [27] [28]). Fig. 4 also shows that for this set of running conditions the magnitude of *K* is mainly influenced by the quantity of vapor, as indicated by the cavitation numbers, and not by the shedding mechanism.

Simulation results at two running conditions (Table 2) were used to make detailed comparisons with the corresponding experimental results. The CFD results in the following section show that both the re-entrant jet and condensation shock shedding mechanisms were achieved. Moreover, they were achieved with pressure drops that matched the experiments for the flow rates used. This is considered the important factor, even though a higher downstream pressure was used in the CFD to guide the amount of cavitation produced. Regarding the shedding frequency, that of the condensation shock shedding mechanism agreed well with the experiments. The frequency of the re-entrant jet shedding mechanism showed some discrepancy. This is strongly linked to the trend shown in Fig. 3: the St_d increases by 100% for a 0.2 change in *CN,* or 0.1 change in σ, indicating an extreme sensitivity of the shedding frequency to the level of cavitation. Hence, the discrepancy in the re-entrant jet shedding frequency is likely explained by this sensitivity, along with cycle to cycle variations and the uncertainties in both the experimental and CFD results.

Table 2 – Running conditions and results for the cases studied in detail.

		Flow rate (l/s)	Δp (kPa)	p_d (kPa)	f (Hz)	St_d	*K*	*CN*	σ
Re-entrant jet	Experiment	2.95	28	80	192	0.24	0.31	0.36	0.86
	CFD	2.94	28	101	250	0.31	0.32	0.29	1.1
Condensation shock	Experiment	2.99	85	26	46	0.056	0.90	3.6	0.25
	CFD	2.99	86	40	43	0.053	0.91	2.2	0.41

3.2- Re-entrant jet vapor shedding mechanism

In Fig. 5, frames of high-speed videos from experiments by Hogendoorn [24] and Jahangir et al [25] are compared with analogous CFD results for re-entrant jet shedding. The first two columns show that vapor structures simulated closely match those of the experiment. The third column shows the axial velocity on the mid-plane, which further illustrates the detail of the vapor shedding and confirms that the re-entrant jet shedding mechanism is well captured by the CFD results. At the start of each cycle, the vapor forms as a toroid at the wall of the Venturi, immediately downstream of the throat (t_0 + 2ms). With time, this cavitating annular region extends downstream, and a re-entrant jet forms at the closure region (t_0 + 4ms, blue shade in column 3) detaching the cavitation at the wall. Separation in a boundary layer is caused by a local adverse pressure gradient, together with sufficiently low velocity at the wall. A re-entrant flow then forms at the separation point. Clearly, an adverse pressure gradient exists at this time, stemming from the cavitating region and the

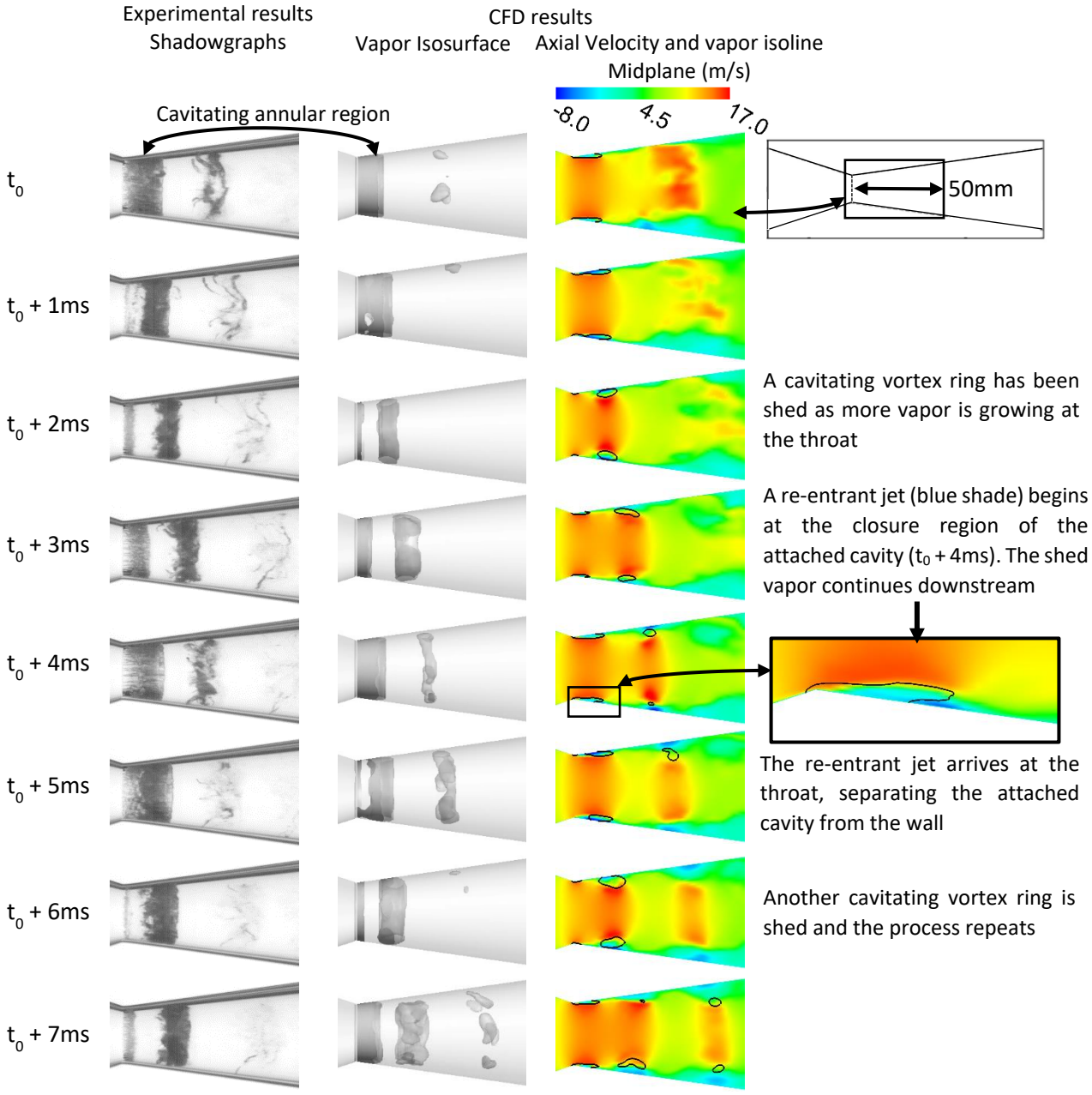

Fig. 5 – Re-entrant jet vapor shedding cycle. Left: experimental high-speed shadowgraphy. Center: CFD Isosurface vapor volume fraction at 10%. Right: color - axial velocity; black isoline - vapor volume fraction at 10% on the mid-plane. See Table 2 for running conditions.

expanding geometry downstream of the Venturi throat. This, together with the low velocity at the wall as seen in Fig. 5, results in separation of the boundary layer and the attendant re-entrant flow. As this re-entrant jet reaches the throat, the vapor detaches completely and is shed downstream as a cavitating vortex ring (t_0 + 6ms) and the process repeats. Some cycle to cycle variation can be seen in Fig. 5 of both the experimental and simulation results. This instability is likely connected with the sensitivity to the running conditions.

3.3 - Condensation shock vapor shedding mechanism

The first and second columns in Fig. 6 compare frames of a high-speed video from experiments by Hogendoorn [24] and Jahangir et al [25] with analogous CFD images for condensation shock shedding. They demonstrate good agreement in timing and in the distribution of the vapor between the experimental and CFD results. The third column in Fig. 6 shows the axial velocity on the mid-plane, which highlights the back flow that develops

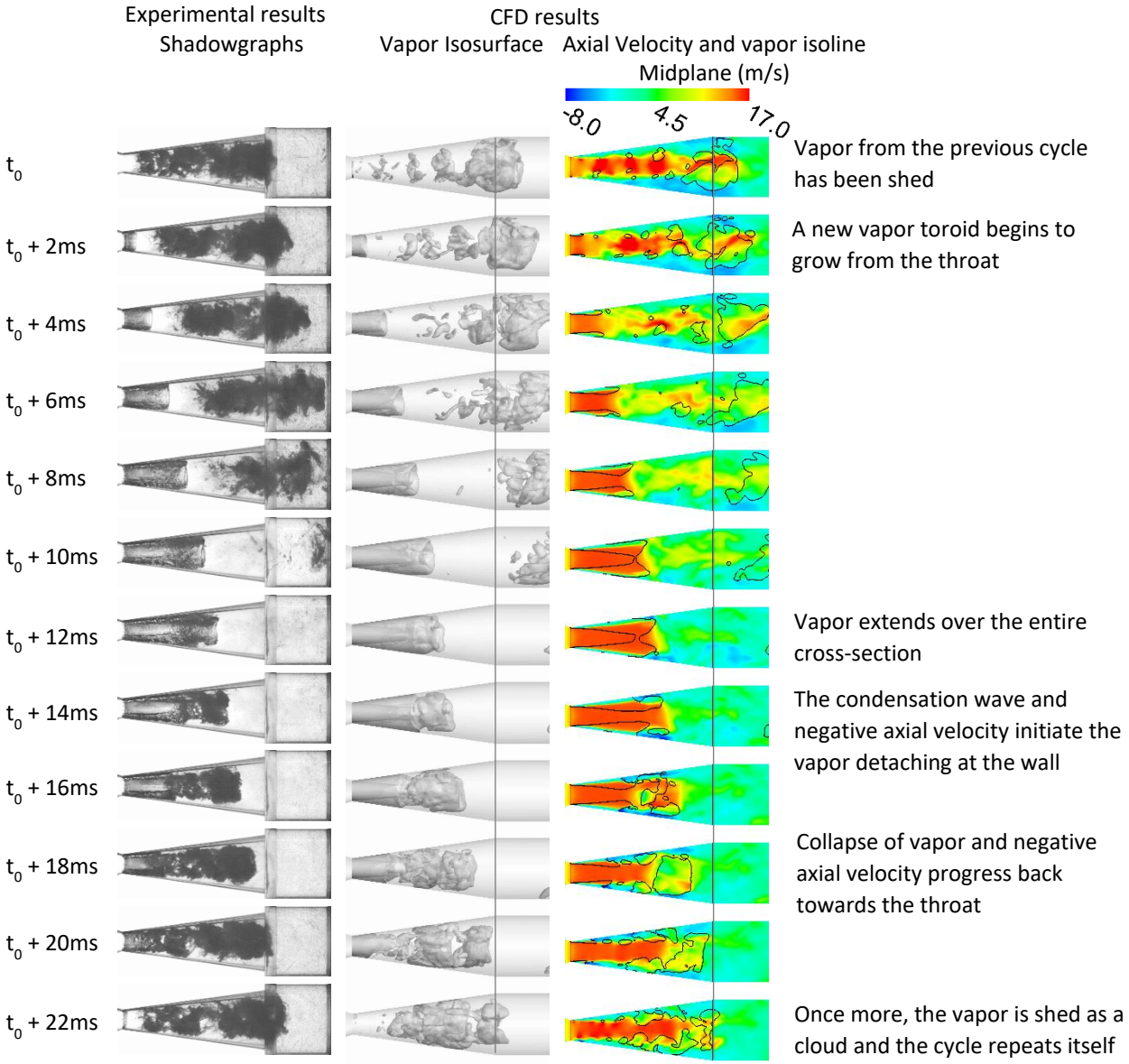

Fig. 6 – Condensation shock vapor shedding cycle. Left: experimental high-speed shadowgraphy, dark grey indicating vapor. Center: CFD Isosurface vapor volume fraction at 10%. Right: color - axial velocity on the mid-plane; black isoline - vapor volume fraction at 10%. See Table 2 for running conditions. Note that in the experiment there is a slightly distorted view in the section after the Venturi. This is due to the exterior shape in the downstream section and not a step in the internal geometry.

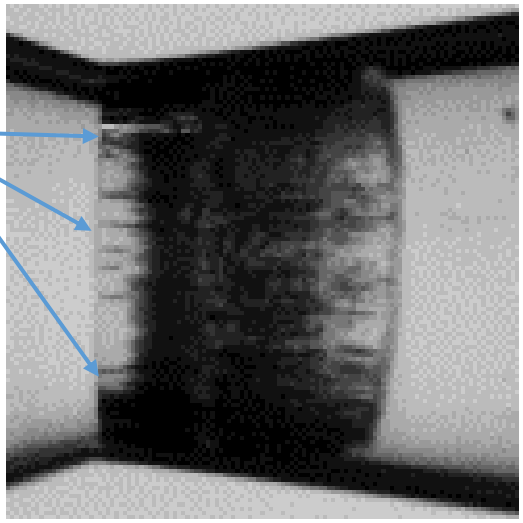

Fig. 7 – Details of cavitation from experiment: enlarged and enhanced section at t_0 + 2ms of Fig. 6.

during the shedding process. The images show that the cavitation grows from the throat (t_0 + 2ms to t_0 + 10ms) and extends considerably further than in the re-entrant jet case.

By frame t_0 + 12ms, the downstream cloud of previously shed vapor has collapsed. This creates a pressure wave that propagates upstream, back to the trailing edge of the attached vapor and triggers the condensation front, which coincides with the appearance of a backflow along the wall (column 3, Fig. 6). The condensation front progressively detaches the vapor at the wall until it reaches the throat, when the whole vapor structure is shed and convected downstream as a cloud.

A close study of the experimental and CFD vapor images reveals that there is a small difference in the cavitation structure close to the throat: in the experiment, the cavitation initiates as streaks [1]. This streak cavitation (Fig. 7) only occurs over a very short distance and is associated with imperfections in the surface finish of the component [46]. The geometry in the CFD is perfectly smooth and does not produce this streak cavitation structure.

The shedding process is further illustrated in Fig. 8, which shows the liquid volume fraction, condensing $d\rho/dt$ (positive values of $d\rho/dt$) and evaporating $d\rho/dt$ (absolute values of negative $d\rho/dt$). As noted in Fig. 6, the first column confirms that the vapor forms in a toroid just downstream from the throat, but later extends across the entire diameter. Moreover, the progress of the condensation front as it travels back towards the throat is revealed by the high values of condensing $d\rho/dt$ (second column) at the trailing edge of the attached cavity (highlighted at t_0 + 15ms). As expected, this tracks the negative velocity in the recirculating flow at the walls, as shown in Fig. 6. Some further condensation and evaporation can be seen within the main body of cavitation. Although higher values of $d\rho/dt$ can be caused by vapor rapidly traveling across cells rather than collapsing or expanding, this is not the case here. Fig. 6 shows there are only low velocities in regions of high $d\rho/dt$.

The images with vapor isoline indicate that the vapor grows from the throat in an annular region close to the walls, and then extends over the entire cross section of the Venturi. It is well known that cavitation in the flow can create the condition in which the acoustic speed in the two-phase mixture falls well below that for each of the single phases [34], enabling supersonic flow. The Rankine-Hugoniot jump condition, originally derived for one-dimensional flow, can be used to identify if the condensation wave does indeed represent a shock front and also computes its velocity [17] [47] [48]. The Rankine-Hugoniot condition is given as:

$$\begin{bmatrix} \rho u \\ \rho u^2 + p \end{bmatrix}_{pre,post} = \mathrm{s} \cdot \begin{bmatrix} \rho \\ \rho u \end{bmatrix}_{pre,post} \qquad \text{Eq. 10}$$

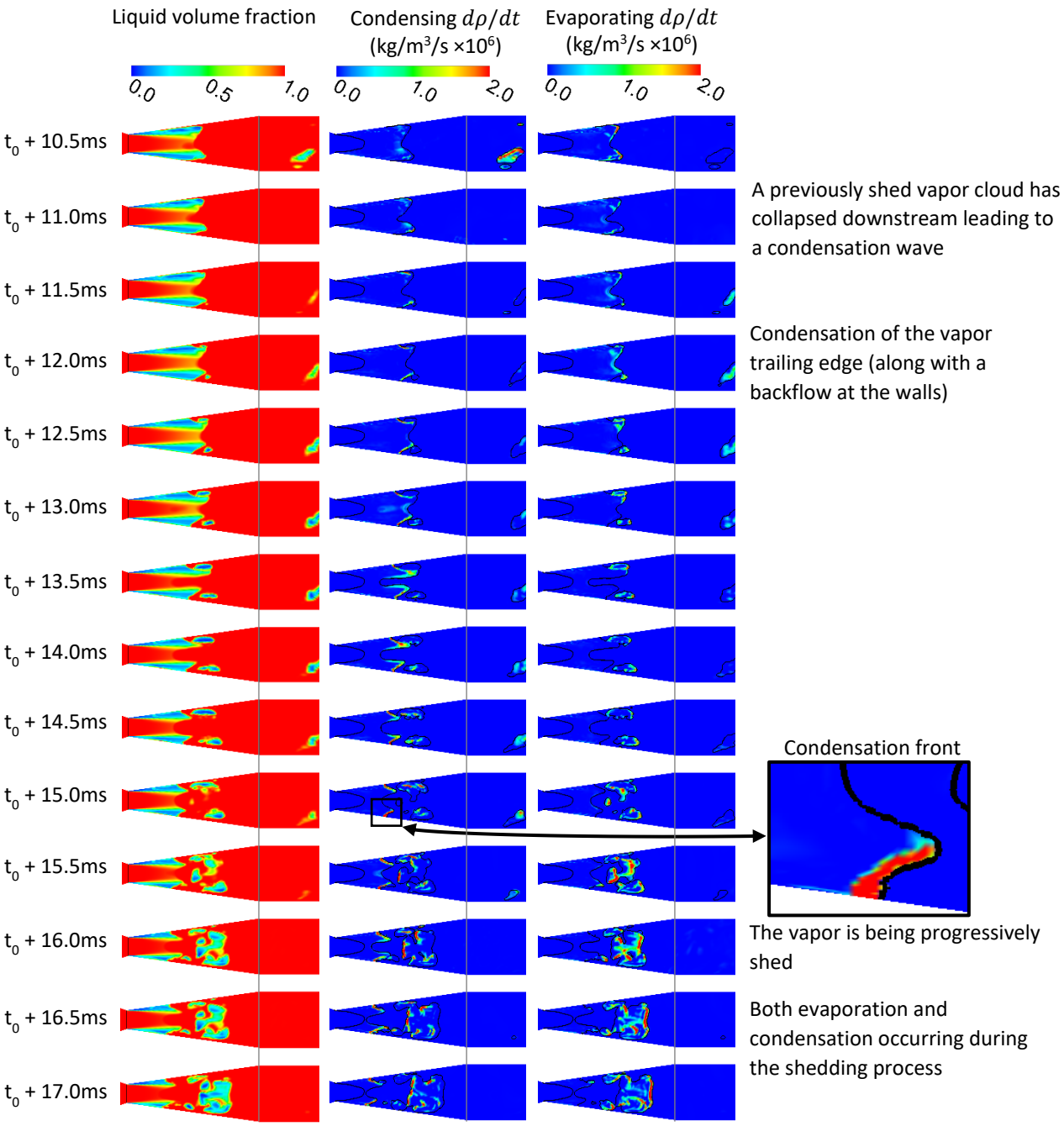

Fig. 8 – Part cycle of condensation shock vapor shedding as the condensation wave travels up the attached cavity. CFD mid-plane values. Left: vapor volume fraction. Middle: condensing $d\rho/dt$. Right: evaporating $d\rho/dt$. Isoline - vapor volume fraction at 1%. See Table 2 for running conditions.

where s is the wave propagation speed and u is the axial velocity component. The subscripts pre and post denote pre- and post-shock and $[\cdot]_{pre,post} = (\cdot)_{pre} - (\cdot)_{post}$. The density, axial velocity and pressure values in Table 3 are taken at pre- and post-shock locations at t_0 + 13.5ms (Fig. 9). The values do indeed satisfy the Rankine-Hugoniot jump condition with a shock propagation speed of 4.2m/s, which agrees with the rate of 4.25m/s calculated from the frames in Fig. 10.

Table 3 – Pre- and post-shock conditions for the Rankine-Hugoniot analysis.

	Density (kg/m³)	Velocity (m/s)	Pressure (Pa)
Pre-shock	158.5	3.84	1,311
Post-shock	998.8	-2.91	10,070

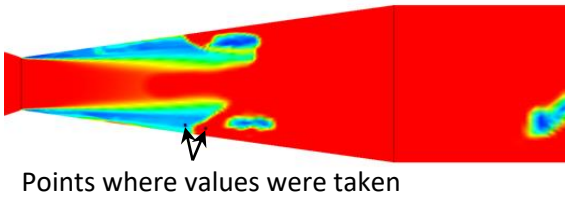

Fig. 9 – Above: Locations where values were taken to test the Rankine-Hugoniot jump condition at t_0 + 13.5ms.

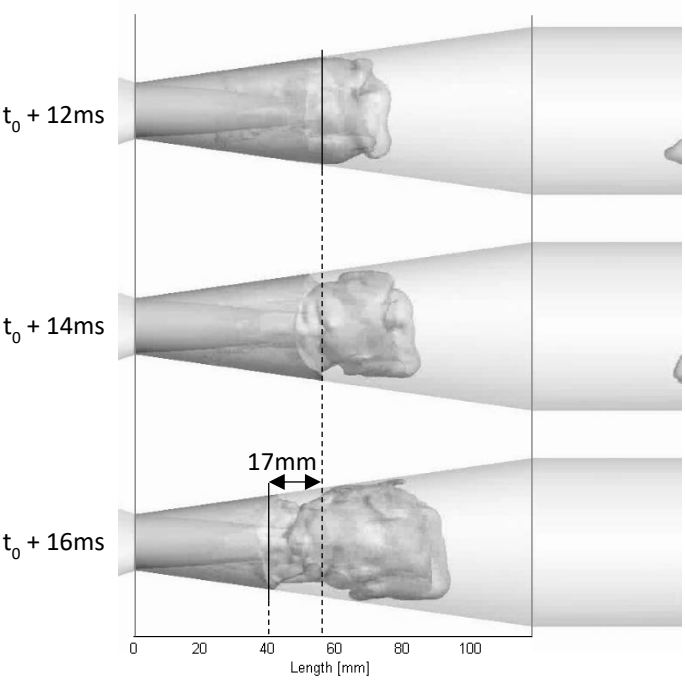

Fig. 10 – Right: Details from Fig. 7 of cavitation from CFD results used to calculate the average shock propagation speed for this time range.

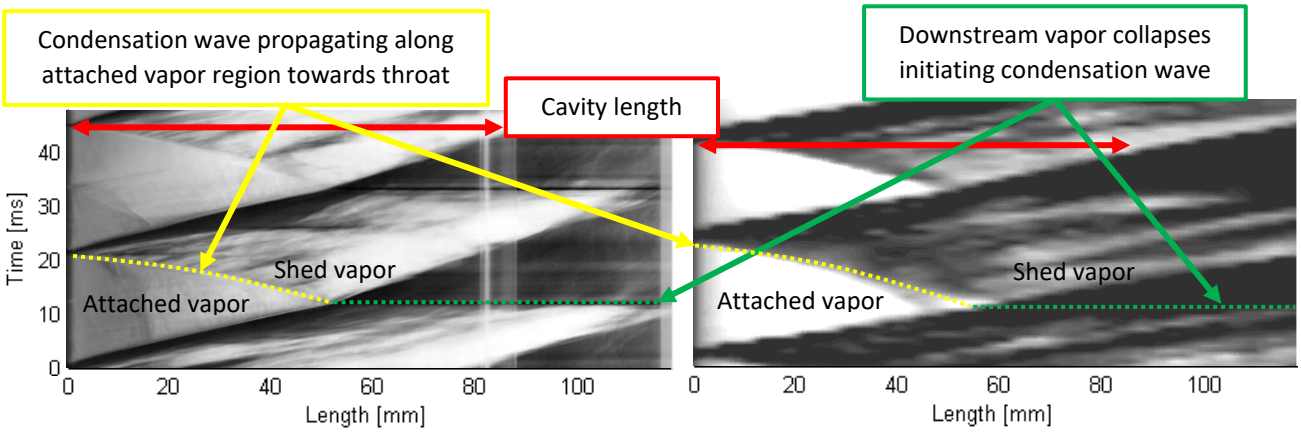

Fig. 11 – Condensation shock vapor shedding: x-t plot of experimental results (left) and CFD results (right). Colors are inverted from previous figures (light gray indicates vapor). Grayscale levels are approximate and do not indicate precise level of vapor. See Table 2 for running conditions. Experimental image reproduced with permission from J. Multiphase Flow. 106, (2018). Copyright 2020 Elsevier

Jahangir et al [25] produced a space-time (x-t) plot from the experimental data. A similar process was repeated with corresponding CFD data using total vapor fraction. Fig. 11 shows the x-t plots constructed from the experimental and CFD results. The cavity lengths (red arrows) agree well, and the condensation and shedding processes occur in a similar manner. Both x-t plots show that shed vapor collapses downstream (green lines). This triggers the condensation wave (yellow curved lines) that travels up the attached vapor to begin a new shedding process.

Finally, 2D experimental time-averaged X-ray images of the cavitating Venturi nozzle were reconstructed using CT to produce a pseudo 3D numerical representation of the averaged vapor content [26]. The X-ray images were taken over 60 seconds (2700 shedding cycles) and captured the projected average of cavitation in the Venturi nozzle (Fig. 12), with the light grey representing vapor. This X-ray data was then reconstructed using CT to show the average vapor distribution at different planes (further examples of CT reconstruction can be found in [49] [50]).

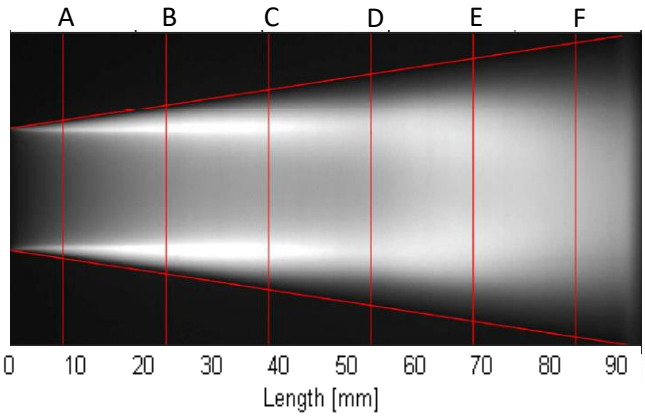

Fig. 12 – Experimental time-averaged X-ray results in the condensation shock regime. Letters indicate where the CT slices were taken. The length covers 93mm. Experimental image reproduced with permission from J. Multiphase Flow. 120, (2019). Copyright 2020 Elsevier.

In order to compare with the averaged CT slices, the CFD results for the vapor volume fraction were averaged over 22 shedding cycles (0.5 seconds). Fig. 13 presents experimental CT results compared with CFD images and shows very good agreement overall.

There is a minor difference in locations A and B, near the throat of the Venturi, where the experimental CT slices show a layer of liquid against the wall, and a higher concentration of vapor adjacent to that. The averaged CFD results show a lower concentration of vapor and it is distributed up to the wall, with no outer ring of liquid. As the CFD predicts a larger distribution of vapor, the overall volume of vapor is consistent with the experiment. These differences at locations A and B are most likely connected to streak cavitation, as discussed earlier (Fig. 7). In the experiment, streak cavitation occurs for a very short distance downstream of the throat, which is not reproduced in the perfectly smooth geometry of the CFD. So in the experiment, the cavitation is intermittent around the throat circumference. These streaks are also likely to be unsteady (some evidence of this in the frames in Fig. 6). Moreover, measurement errors with CT reconstruction will be more significant in the tube periphery, as the X-ray line of sight only passes through a very small volume of mixture. These factors are likely why the CT processing has interpreted total liquid next to the wall.

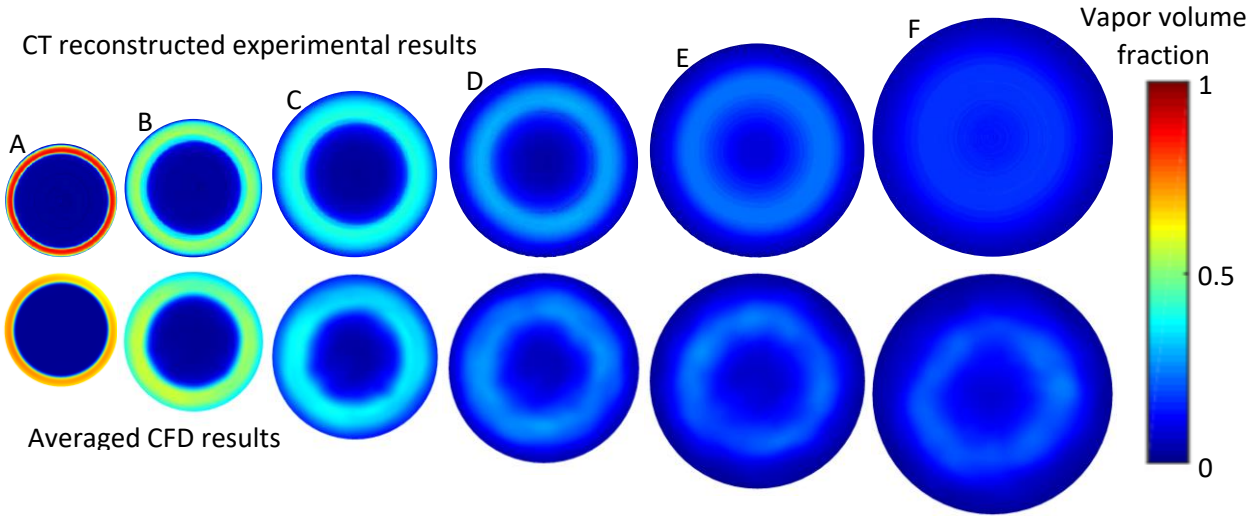

Fig. 13 – Condensation shock mechanism: comparison of the average vapor fraction from experimental (top, [26]) and CFD results (bottom). See Table 2 for running conditions. Experimental image reproduced with permission from J. Multiphase Flow. 120, (2019). Copyright 2020 Elsevier.

4 – Conclusion

The vapor shedding mechanisms of cavitating flows in an axisymmetric Venturi nozzle were investigated with CFD simulations and the results compared with those of relevant experiments. New analysis of the quantitative results with regards to the Strouhal number and loss factor revealed coherent trends and showed the good overall agreement between the experiments and CFD over a wide range of running conditions. Moreover, it was concluded that the *CN* cavitation number was the more appropriate parameter for use with internal, three-dimensional geometries involving a pressure drop. Hence, analysis with *CN* is recommended for future similar work. Two running conditions were studied in detail with CFD, and the results confirmed the findings from experiment, that re-entrant jet and condensation shock were the dominant vapor shedding mechanisms.

Analysis of the full data set over the range of running conditions provided insight into the conditions under which the different vapor shedding mechanisms occurred and revealed the extreme sensitivity of the re-entrant jet mechanism, which only occurs over a very narrow range of running conditions. This signified that a small change in settings would produce a large change in the shedding frequency for this mechanism, which is why it has been difficult to simulate reliably in previous research.

For both shedding mechanisms, the details and development of the simulated vapor structures during a shedding cycle closely matched those of the experiments and the measured pressure drop was achieved as well. Moreover, the CFD results provided detail of the flow mechanisms that cannot be extracted from the experiments. Finally, a comparison of average vapor fraction was conducted using CT slices from the experiments. This demonstrated overall good agreement with the averaged CFD results and, together with the other results, confirmed the reliability of the CFD simulations. From this, the understanding of cavitation and shedding mechanisms, which can affect flow stability, spray break-up and erosion in orifices, has been expanded.

Acknowledgements

The research leading to these results has received funding from European Union's Marie Sklodowska-Curie Innovative Training Network (ITN) MSCA-ITN-2014-ETN, under REA grant agreement number 642536.

Data availability

Raw data were generated at the City, University of London facility. Derived data supporting the findings of this study are available from the corresponding author upon reasonable request.

References

[1] C. Brennen, Cavitation and Bubble Dynamics, Oxford University Press, 1995.

[2] C. Soteriou, R. Andrews and M. Smith, "Further studies of cavitation and atomization in diesel injection," *SAE Technical Paper 1999-01-1486,* 1999.

[3] J.-P. Franc and J.-M. Michel, Fundamentals of Cavitation, New York: Kluwer Academic Publishers, 2005.

[4] M. Brunhart, C. Soteriou, C. Daveau, M. Gavaises, P. Koukouvinis and M. Winterbourn, "Investigation on the removal of the cavitation erosion risk in a control orifice inside a prototype diesel injector," in *IMechE Fuel Systems*, London, 2018.

[5] T. Melissaris, N. Bulton and T. van Terwisga, "On cavitation aggresiveness and cavitation erosion on marine propellers using URANS method," in *10th International Cavitation Symposium*, Baltimore, 2018.

[6] R. T. Knapp, "Recent investigations of the mechanics of cavitation and cavitation damage," *Trans. ASME,* vol. 77, no. 5, pp. 1045-1054, 1955.

[7] R. A. Furness and S. P. Hutton, "Experimental and theoretical studies of two-dimensional fixed-type cavities," *J. Fluids Eng.,* pp. 515-521, 1975.

[8] E.-J. Foeth, T. J. C. van Terwisga and C. van Doorne, "On the collapse structure of an attached cavity on a three-dimensional hydrofoil," *Trans. ASME J. Fluids Eng.,* vol. 130, no. 7, 2008.

[9] T. Pham, F. Larrarte and D. Fruman, "Investigation of unsteady sheet cavitaiton and cloud cavitaiton mechanisms," *J. FLuids Eng.,* vol. 121, no. 2, pp. 289-296, 1999.

[10] C. Stanley, T. Barber and G. Rosengarten, "Re-entrant jet mechanism for periodic cavitation shedding in a cylindrical orifice," *Int. J. Heat Fluid Flow,* vol. 50, pp. 169-176, 2014.

[11] Y. Kawanami, H. Kato, H. Yamaguchi, M. Tanimura and Y. Tagaya, "Mechanism and control of cloud cavitaiton," *J. Fluids Eng.,* vol. 119, no. 4, pp. 788-794, 1997.

[12] J. Jakobsen, "On the mechanism of head breakdown in cavitating inducers," *J. Basic Eng.,* vol. 86, no. 2, pp. 291-305, 1964.

[13] I. J. Campbell and A. S. Pitcher, "Shock waves in a liquid containing gas bubbles," *Proceedings of the Royal Society of London. Series A, Mathematical and Physical Sciences,* vol. 243, no. 1235, pp. 534-545, 1958.

[14] G. E. Reisman, Y. C. Wang and C. E. Brennen, "Observations of shock waves in cloud cavitation," *J. Fluid Mech.,* vol. 355, p. 255–283, 1998.

[15] K. R. Laberteaux and S. L. Ceccio, "Partial cavity flows. Part 1. Cavities forming on models without spanwise variation," *J. Fluid Mech.,* vol. 431, p. 1–41, 2001.

[16] C. Wang, B. Huang, G. Wang, M. Zhang and N. Ding, "Unsteady pressure fluctuation characteristics in the process of breakup and shedding of sheet/cloud cavitaiton," *Int. J. Heat Mass Transf.,* vol. 114, pp. 769-785, 2017.

[17] B. Budich, S. Schmidt and N. Adams, "Numerical simulation and analysis of condensation shocks in cavitating flow," *J. Fluid Mech.,* vol. 838, pp. 759-813, 2018.

[18] M. A. Arabnejada, A. Amini, M. Farhat and R. E. Bensow, "Numerical and experimental investigation of shedding mechanisms from leading-edge cavitation," *Int. J. of Multi. Flow,* vol. 119, pp. 123-143, 2019.

[19] R. Arndt, C. Song, M. Kjeldsen, J. He and A. Keller, "Instability of partial cavitation: a numerical/experimental approach," in *23rd Symposium on Naval Hydrodynamics*, Val deReuil, 2000.

[20] H. Ganesh, S. Makiharju and S. Ceccio, "Bubbly shock propagation as a mechanism for sheet-to-cloud transition of partial cavities," *J. Fluid Mech.,* vol. 802, pp. 37-78, 2016.

[21] T. Trummler, S. Schmidt and N. Adams, "Investigation of condensation shocks and re-entrant jet dynamics in a cavitating nozzle flow by Large-Eddy Simulation," *Int. J. Multiphase Flow,* vol. 125, 2020.

[22] A. Sou, B. Bicer and A. Tomiyama, "Numerical simulation of incipient cavitation flow in a nozzle of fuel injector," *Computers and Fluids,* vol. 103, pp. 42-48, 2014.

[23] B. Bicer and A. Sou, "Numerical models for simulation of cavitation in diesel injector nozzles," *Atomization and Sprays,* vol. 25, no. 12, pp. 1063-1080, 2015.

[24] W. Hogendoorn, "Cavitation: Experimental investigation of cavitation regimes in a converging-diverging nozzle," Delft University of Technology, Master Thesis, 2017. http://resolver.tudelft.nl/uuid:823a18f0-66a8-4ffd-a688-c3dadf62c4da.

[25] S. Jahangir, W. Hogendoorn and C. Poelma, "Dynamics of partial cavitation in an axisymmetric converging-diverging nozzle," *Int. J. of Multiphase Flow,* vol. 106, no. 34, 2018.

[26] S. Jahangir, E. C. Wagner, R. F. Mudde and C. Poelma, "Void fraction measurements in partial cavitation regimes by X-ray computed tomography," *Int. J. of Multiphase Flow,* vol. 120, no. 103085, 2019.

[27] B. Cointe, "Cavitation: CFD analysis of cavitaiton dynamics in a converging-diverging nozzle," Delft University of Technology, Master Thesis, 2018. http://resolver.tudelft.nl/uuid:af624f59-e477-4dbe-a5b7-39902a0b1b99.

[28] P. Gorkh, S. Schmidt and N. Adams, "Numerical investigation of cavitation-regimes in a converging-diverging nozzle," in *10th International Symposium on Cavitation (CAV18)*, Baltimore, 2018.

[29] G. Chen, G. Wang, C. Hu, B. Huang, Y. Gao and M. Zhang, "Combined experimental and computational investigation of cavitation evolution and excited pressure fluctuation in a convergent-divergent channel," *Int. J. Multiphase Flow,* vol. 72, pp. 133-140, 2015.

[30] H. Zhang, Z. Zuo, K. Morch and S. Liu, "Thermodynamic effects on venturi cavitation characteristics," *Physics of Fluids,* vol. 31, no. 097107, 2019.

[31] B. Stutz and J.-L. Reboud, "Two-phase flow structures of sheet cavitation," *Physics of Fluids,* vol. 9, no. 12, pp. 3678-3686, 1997.

[32] P. Koukouvinis, H. Naseri and M. Gavaises, "Performance of turbulence and cavitation models in prediction of incipient and developed cavitation," *Int. J. of Engine Research,* vol. 18, 2016.

[33] N. Kyriazis, P. Koukouvinis and M. Gavaises, "Numerical investigation of bubble dynamics using tabulated data," *Int. J. of Multiphase Flow,* vol. 93, pp. 158-177, 2017.

[34] G. Wallis, One-dimensional Two-phase Flow, McGraw-Hill, 1969.

[35] F. Menter and Y. Egorov, "The Scale-Adaptive Simulation Method for Unsteady Turbulent Flow Predictions . Part 1 : Theory and Model Description," *Flow Turbulence Combustion,* vol. 85, pp. 113-138, 2010.

[36] Ansys, Inc., "Ansys Fluent Theory Guide," SAS IP, Canonsburg, PA., 2013.

[37] T. Colonius, "Modeling artificial boundary conditions for compressible flow," *Ann. Rev. Fluid Mech.,* vol. 36, pp. 315-345, 2004.

[38] A. Gnanaskandan and K. Mahesh, "Large Eddy Simulation of the transition from sheet to cloud cavitation over a wedge," *Int. J. of Multiphase Flow,* vol. 83, pp. 86-102, 2016.

[39] Delphi Technologies, *Internal documents.*

[40] W. Bergwerk, "Flow patterns in diesel nozzle spray holes," *Proc. of the Inst. of Mech Eng.,* vol. 173, no. 25, pp. 655-660, 1959.

[41] J. Tullis, "Cavitation guide for control valves," US Nuclear Regulatory Commission, Washington, 1993.

[42] M. Gavaises, D. Papouluas, A. Andritotis and E. Giannadakis, "Link between cavitation development and erosion damage in diesel injector nozzles," *SAE Technical Paper 2007-01-0246,* 2007.

[43] M. Gavaises, A. Andriotis, D. Papoulias, N. Mitroglou and A. Theodorakakos, "Characterization of string cavitation in large-scale Diesel nozzles with tapered holes," *Physics of Fluids,* vol. 21, no. 5, 2009.

[44] C. Soteriou, R. Andrews and M. Smith, "Direct Injection Diesel Sprays and the Effect of Cavitation and Hydraulic Flip on Atomization," *SAE Technical Paper,* 1995.

[45] J. Rose, J. Cooper and H. Spiers, Technical data on fuel, London: Scottish Academic Press, 1977.

[46] C. Soteriou, "Some flow effects of cavitation inside Diesel injectors," in *ILASS*, Chania, 2013.

[47] W. Rankine, "On the thermodynamic theory of waves of finite longitudinal disturbances," *Phil. Trans. Roy. Soc. London,* vol. 160, pp. 277-286, 1870.

[48] P. Hugoniot, "Mémoire sur la propagation du movement dans les corps et plus specialement dans les gaz parfaits, 1-2 Partie," *J. Ecole Polytech,* vol. 58, pp. 1-125, 1889.

[49] N. Mitroglou, M. Lorenzi, M. Santini and M. Gavaises, "Application of X-ray micro-computer tomography on high speed cavitating diesel fuel flows," *Exp. Fluids,* vol. 57, no. 11, 2016.

[50] D. Bauer, F. Barthel and U. Hampel, "High-speed X-ray CT imaging of a strongly cavitating nozzle flow," *J. Phys. Commun,* vol. 2, no. 7, 2018.